# Virtual indentation of the empty capsid of the minute virus of mice using a minimal coarse-grained model

Manuel Martín-Bravo, Jose M. Gomez Llorente,* and Javier Hernández-Rojas
*Departamento de Física and IUdEA, Universidad de La Laguna, 38200 Tenerife, Spain*

(Received 20 June 2023; accepted 2 January 2024; published 6 February 2024)

A minimal coarse-grained model for $T = 1$ viral capsids assembled from 20 protein rigid trimers has been designed by extending a previously proposed form of the interaction energy written as a sum of anisotropic pairwise interactions between the trimeric capsomers. The extension of the model has been performed to properly account for the coupling between two internal coordinates: the one that measures the intercapsomer distance and the other that gives the intercapsomer dihedral angle. The model has been able to fit with less than a 10% error the atomic force microscopy (AFM) indentation experimental data for the empty capsid of the minute virus of mice (MVM), providing in this way an admissible picture of the main mechanisms behind the capsid deformations. In this scenario, the bending of the intercapsomer dihedral angle is the angular internal coordinate that can support larger deformations away from its equilibrium values, determining important features of the AFM indentation experiments as the elastic constants along the three symmetry axes of the capsid and the critical indentations. From the value of one of the parameters of our model, we conclude that trimers in the MVM must be quite oblate tops, in excellent agreement with their known structure. The transition from the linear to the nonlinear regimes sampled in the indentation process appears to be an interesting topic for future research in physical virology.

DOI: 10.1103/PhysRevE.109.024402

## I. INTRODUCTION

Physical virology is an expanding field of research that uses theoretical methods and experimental techniques of physics to understand the principles behind the structure, properties and processes that characterize the viruses. Viruses stand out from other infectious agents, like viroids, by the presence of a capsid, i.e., a protein shell that encloses the genetic material (RNA or DNA), and plays an essential role in the delivery of this material into the host cell. The capsid has a well defined geometrical structure and consists of copies of a small number of proteins (only one in the simplest cases). In most viruses, the capsid is icosahedral (symmetry point group $I$). This is the highest symmetry that a system composed of a finite number of asymmetric building blocks, such as proteins, can have. Progress in this field is providing relevant insights in hot topics of nanobiotechnology such as the development of viral-based drug delivery strategies or the design of unique synthetic protein cages [1–3].

Common experimental techniques in physical virology are mass spectroscopy, transmission electron microscopy, and atomic force microscopy (AFM). All of them provide structural details and the last two are imaging techniques. In addition, AFM nanoindentation schemes have been developed to study the mechanical properties of viruses [4–6]. These schemes use the AFM cantilever as a force transducer that can manipulate the virus at the atomic scale. The result is a force-displacement curve. After the tip makes contact with the capsid, the force increases almost linearly. One can then define the spring constant of the virus as the slope of the cantilever deflection on the virus. When the indentation is large enough, the elastic limit is surpassed and mechanical failure is observed in the virus particle. This event determines what is known as the critical indentation. A multitude of AFM experiments have been carried out *in vitro* [4,7–13], *in silico* [14–24], and in mixed forms [5,25–27]. Reviews discussing these studies are also available [28–32].

Of interest to our present paper are the AFM experimental works on the minute virus of mice (MVM) [9,12,33]. Using a combination of AFM and TEM techniques, Medrano *et al.* [33] found, in agreement with previous studies [34–37], that the proteins of MVM capsid arrange *in vitro* to form trimers that latter assemble into empty $T = 1$ icosahedral capsids of $\sim$25 nm in diameter. These authors determined the spring force constants of the MVM empty capsid for indentations along its three symmetry axes (twofold, threefold, and fivefold) and the average critical indentation [9,12]. At critical indentation, trimers start to detach from the capsid.

Physical virology uses theoretical approaches from the perspective of many fields in physics such as thermodynamics, statistical physics, kinetics, mechanics, and elasticity. Computer modeling is a powerful tool in all these approaches. Large all-atom simulations of some viral properties and processes have been undertaken in the last decade. However, the theoretical understanding of the more universal physical properties found in viruses requires us to relinquish the details of the molecular scale involved in these simulations and develop coarse-grained models that incorporate the relevant features [14,17–21,23,24,26,38–65]. Some of these models describe the capsid as a continuous medium to explain its mechanical and elastic properties [27,59–61,63]. Others

*Corresponding author: jmgomez@ull.edu.es

 

use spring nets for this purpose [22,56–59,66,67]. On the other hand, most discrete models represent the capsid as a set of a small number of rigid subunits of one or more different classes and propose a binary interaction potential energy between them [17–21,23,24,26,43,48–51,53–55,64,68–70]. These models provide potential energy landscapes [71] whose global minima reproduce the observed structures of the capsids. Moreover, theoretical analyses of this landscape and its connection with the kinetics of the self-assembly process can also be carried out.

One of these discrete coarse-grained models of a viral capsid, whose rigid subunits are axially symmetric bodies representing pentamers and hexamers, has been used to simulate virtual AFM indentations of empty capsids [62]. In this paper, the authors try to mimic the indentation process carrying out Brownian dynamics simulations. The capsomers are described as axisymmetric rigid bodies separated into pentamers and hexamers, with mutual binary interactions depending on the capsomer type, the separation distance, and on the other three internal angular coordinates. With this model, the authors obtain indentation curves for a $T = 7$ virus capsid along the threefold, twofold, and fivefold directions, showing qualitative agreement with the experiments.

When the relevant structural subunits of the capsid (capsomers) are not pentamers and hexamers, its nonaxial symmetry must be explicitly included in the model. This is the case for the MVM capsid, which is known to self-assemble from trimers [33]. In any case, a viral capsomer is not an axially symmetric body, in which case an additional degree of freedom is required to determine its configuration, and that may be relevant in the mechanical properties of the capsid.

MVM is too small to hope that continuous or discrete elastic models or even discrete models based on axisymmetric units, particularly when these are trimers [62,68], can quantitatively account for all the details the AFM indentation process. In the present paper, a finite-element minimal coarse-grained model of viral icosahedral capsids previously proposed and generalized to fit the low-frequency normal-mode spectrum of the satellite tobacco necrosis virus capsid (a $T = 1$ capsid) [64], will be adapted to quantitatively reproduce the indentation data from the AFM experimental work on the MVM, also a $T = 1$ capsid [9,12,33], and to provide predictions for this process. In Sec. II, the coarse grained model is presented. Virtual indentations are performed in Sec. III. By fitting them to the experimental data, the optimal model parameters are obtained and a neat physical picture of the indentation process emerges. The conclusions of our paper are collected in Sec. IV.

## II. THE MODEL

This paper uses a coarse-grained model of the capsid which is assumed to be made up of rigid subunits. Thus, six degrees of freedom are required to fix the location and orientation of each one of them. The MVM is the subject of this paper. As mentioned in the Introduction, the intrinsic subunits in this case are trimers. We will write the total interaction energy of the empty capsid as a sum of pairwise anisotropic interactions between trimers. We will use a simplified version of the binary interaction presented in a previous work to fit the normal mode

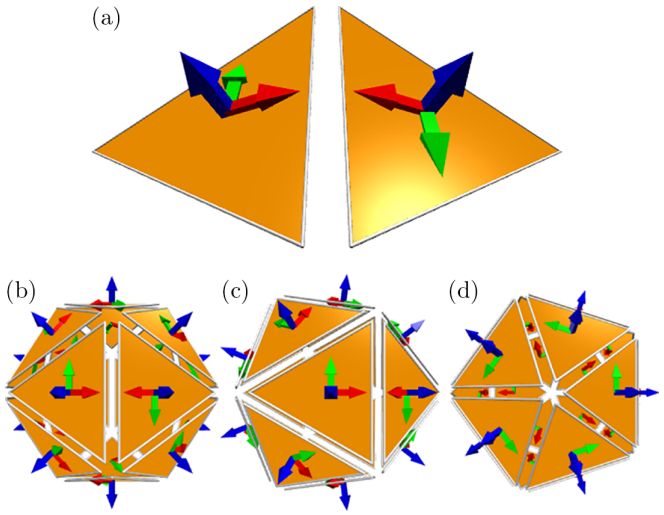


FIG. 1. Equilibrium configuration of a pair of trimers in (a) and of a full capsids in (b)–(d). Arrows represent the proper axis of each trimer: $\mathbf{v}_z$ is perpendicular to the trimer, $\mathbf{v}_x$ is perpendicular to both $\mathbf{v}_z$ and one edge, and $\mathbf{v}_y = \mathbf{v}_z \times \mathbf{v}_x$. (b)–(d) show, respectively, the top views along a two-, three-, and fivefold axis of the full capsid. Note that in all cases (a)–(d), any capsomer frame could be rotated an angle $\pm 2\pi/3$ around its proper vector $\mathbf{v}_z$ and the resulting configuration would be equivalent.

frequency spectrum of the satellite tobacco necrosis virus capsid (also a $T = 1$ capsid) [64]. We will retain the lowest order terms of such a multipolar expansion and incorporate relevant nonlinear effects, which will be required for the capsid response to indentation, namely, the binary trimer-trimer interaction is

$$\begin{aligned} V_{ij} = {} & p_0 F_0 \\ & + p_1 F_1 \cdot [1 - \mathbf{v}_{zi}\cdot\mathbf{v}_{zj} + 2(\mathbf{v}_{zi}\cdot\mathbf{n}_{ij})(\mathbf{v}_{zj}\cdot\mathbf{n}_{ij})] \\ & + p_2 F_2 \cdot [(\mathbf{v}_{zi}\cdot\mathbf{n}_{ij} + \cos\theta_e)^2 + (\mathbf{v}_{zj}\cdot\mathbf{n}_{ij} - \cos\theta_e)^2] \\ & + p_3 F_3 \cdot [\mathrm{Re}\{[(\mathbf{v}_{xj} + \mathrm{i}\,\mathbf{v}_{yj})\cdot\mathbf{n}_{ij}]^3 - [(\mathbf{v}_{xi} + \mathrm{i}\,\mathbf{v}_{yi})\cdot\mathbf{n}_{ij}]^3\} \\ & + [1 - (\mathbf{v}_{zi}\cdot\mathbf{n}_{ij})^2]^{3/2} + [1 - (\mathbf{v}_{zj}\cdot\mathbf{n}_{ij})^2]^{3/2}], \end{aligned} \tag{1}$$

where $p_0, \ldots, p_3 > 0$ are four parameters, $F_0, \ldots, F_3$ are four functions to be given below, $\mathbf{n}_{ij}$ is the unitary vector $\mathbf{n}_{ij} = \mathbf{r}_{ij}/r_{ij}$, with $\mathbf{r}_{ij}$ being the intercapsomer position vector from capsomer $i$ to capsomer $j$. The three principal axes of each capsomer $i$ are given, respectively, by the unitary vectors $\mathbf{v}_{xi}$, $\mathbf{v}_{yi}$, and $\mathbf{v}_{zi}$. Parameter $\theta_e$ is given in the header of Table VI and is purely geometrical: it fixes the intended relative orientation of $\mathbf{v}_{zi}$ and $\mathbf{v}_{zj}$ in the equilibrium configuration. Re{} stands for the real part. We offer Fig. 1 to better visualize the equilibrium configurations of two isolated trimers and of the full capsid with 20 trimers.

The binary system of two capsomers (two rigid bodies) requires 12 degrees of freedom. If ones removes the three arbitrary translations and three arbitrary rotations of the reference frame, one obtains the six internal coordinates on which the binary interaction in Eq. (1) can depend.

This interaction has a twofold symmetry axis and, as a consequence, the six internal coordinates of the binary system (two rigid trimers) can be defined as either symmetric (+) or

TABLE I. Dimensionless internal symmetry-adapted coordinates (first column) of a binary system (two rigid trimers) and their intended equilibrium values (second column) to encode a $T = 1$ capsid, with integer $l \in \mathbb{Z}$ and $\theta_e = \arccos(\frac{1}{\varphi\sqrt{3}})$, where $\varphi = \frac{1+\sqrt{5}}{2}$ is the golden ratio.

| Internal coordinates | Equilibrium values |
|---|---|
| $r^+ = r_{ij}/r_e$ | 1 |
| $\phi^+ = \phi_j - \phi_i$ | 0 |
| $\theta^+ = \theta_j - \theta_i$ | $2\theta_e - \pi$ |
| $\chi^+ = \chi_j + \chi_i$ | $\pi \pm \frac{2\pi l}{3}$ |
| $\theta^- = \theta_j + \theta_i$ | $\pi$ |
| $\chi^- = \chi_j - \chi_i$ | $-\pi \mp \frac{2\pi l}{3}$ |

antisymmetric (−) with respect to a rotation of $\pi$ around that axis. These internal coordinates and their equilibrium values are given in Table I. These are the reduced intercapsomer distance $r_{ij}/r_e$ ($r_e$ being the equilibrium distance), which is symmetric, and the appropriate symmetrical and antisymmetrical combinations of Euler angles in the ZYZ convention $(\theta, \phi, \chi)$, as defined in a previous work [64].

The expression in Eq. (1) is the minimal form required to encode a $T = 1$ capsid from 20 trimeric subunits. Such a capsid appears, for properly chosen parameters, as the global minimum of the total interaction potential (the sum of all pairwise binary interactions)

$$V = \sum_{i=1}^{20} \sum_{j=i+1}^{20} V_{ij}, \tag{2}$$

on a quite funneled energy surface landscape. The effect and significance of each of the terms in Eq. (1) are explained in detail in our previous works [64,65].

Formerly, $F_0, \ldots F_3$ were functions of only $r_{ij}$. Now that restriction has been removed to adapt the model beyond the equilibrium region and to closely reproduce the coupling between the radial coordinate $r^+$ and the bending of the intercapsomer dihedral angle $\theta$. This is the angle between the planes containing the $\mathbf{v}_{xi}$ and $\mathbf{v}_{yi}$ vectors of two neighbor trimers, which is given by $\theta = \frac{\pi - \theta^+}{2}$, in terms of the $\theta^+$ internal coordinate. As we will demonstrate later, this $r^+ - \theta^+$ coupling is going to determine the indentation response of the capsid. To model this process, we will define an effective equilibrium distance $\tilde{r}_e$ that depends on the relative orientation of a pair of capsomers, i.e., on their dihedral angle $\theta$, namely,

$$\tilde{r}_e = r_0 + (r_e - r_0)\frac{\sin^2\theta}{\sin^2\theta_e}, \tag{3}$$

where $\sin\theta = \cos\frac{\theta^+}{2}$. The parameter $r_0$ allows capsomers to respond to indentation as either prolate or oblate bodies, when its value is larger or smaller than the intended equilibrium distance $r_e$, respectively. In the first case, $r^+$ increases or decreases as $\theta^+$ does, and in the second case one has the opposite behavior. If $r_0 = r_e$, this coupling disappears as for two spherical subunits (an unlikely situation).

The form in Eq. (3) was checked to be somewhat better than other forms providing similar effects. No realistic capsid response to indentation can be obtained without taking into account these effects. After applying trigonometric identities, we arrive at the expression

$$\sin^2\theta = \tfrac{1}{2}\{1 + (\mathbf{v}_{zi}\cdot\mathbf{n}_{ij})(\mathbf{v}_{zj}\cdot\mathbf{n}_{ij}) + \sqrt{[1-(\mathbf{v}_{zi}\cdot\mathbf{n}_{ij})^2][1-(\mathbf{v}_{zj}\cdot\mathbf{n}_{ij})^2]}\}, \tag{4}$$

which enables us to particularize $F_0, \ldots F_3$ as follows:

$$F_0 = \left(\frac{\tilde{r}_e}{r_{ij}}\right)^{2m} - 2\left(\frac{\tilde{r}_e}{r_{ij}}\right)^{m}, \tag{5a}$$

$$F_1 = F_2 = F_3 = \left(\frac{\tilde{r}_e}{r_{ij}}\right)^{m'm}, \tag{5b}$$

where $m > 0$ and $m' \geqslant 1$. Thus $F_1$, $F_2$, and $F_3$ decay more rapidly than the attractive contribution of $F_0$. $F_0$ generalizes the Lennard-Jones potential and makes it dependent on both the relative position and the relative dihedral orientation of capsomers.

## III. VIRTUAL INDENTATION

### A. The indentation setup

Our interaction model (Sec. II) is interpreted as a free energy; therefore, any thermal, pH, or salinity effect modifies parameters $p_0, \ldots p_3, m, m'$ accordingly and, to some extent, $r_0$ too.

Virtual indentations will be performed along the three symmetry axes of the MVM, i.e., the twofold ($C_2$), threefold ($C_3$), and fivefold ($C_5$) axes. In each case, the direction of the symmetry axis is taken along the $Z$ axis of the laboratory frame. Indentation requires the setup of certain constraints. For that purpose, we consider the top and bottom trimers of the capsid in each of the three orientations, and we refer to them as roof and ground trimers. We have two roof and two ground trimers for the $C_2$ axis, one roof and one ground trimer for the $C_3$ axis and five roof and five ground trimers for the $C_5$ axis.

We impose the indentation constraint that fixes the $z_i$ coordinates of the roof trimers to a particular common value $z_i = z/2$ and in a similar way the $z_i$ coordinates of the ground trimers are fixed to $z_i = -z/2$. The initial value for $z = z_{\max}$, which is the maximum one, corresponds to the free capsid before the indentation process. This value of $z_{\max}$ is different for each of the three orientations (approximately 1.401 $r_e$, 1.309 $r_e$, and 1.114 $r_e$ for the $C_3$, $C_2$, and $C_5$ axes, respectively).

Displacements and overturning of the capsid is prevented differently depending on the indentation axis. For indentations along the $C_3$ axis, both the roof and ground trimers are imposed to have their $x_i$ and $y_i$ coordinates at the origin. When the indentation is practiced along the $C_2$ axis, the initial configuration is chosen so the two roof capsomers and the two floor capsomers have their $x_i$ coordinates at the origin. For indentation along the $C_5$ axis, no additional constraints where imposed. Indentation is carried out by reducing $z$ in the form $z = z_{\max} - h$, where $h$ is the indentation variable. This variable is changed in increments of magnitude $\Delta h = z_{\max}/1000$. At each step, the capsid is relaxed to the closest local minimum of its energy surface satisfying the indentation constraints; the capsid internal energy, $V(h)$, and the force, $F(h) = dV(h)/dh$, are then determined. This virtual indentation is, therefore, an adiabatic process.

TABLE II. Optimal parameters of our model from the fit for displacement and force-driven indentations, with up to two significant figures. Units are given within brackets, with $p_0 = 72.3$ kJ/mol and $r_e = 9.20$ nm.

| Driven by | $m$ | $m'$ | $r_0$ [$r_e$] | $p_1$ [$p_0$] | $p_2$ [$p_0$] | $p_3$ [$p_0$] | $\mathcal{C}$ |
|---|---|---|---|---|---|---|---|
| Displacement | $6.3 \pm 0.3$ | $2.9 \pm 0.3$ | $0.160 \pm 0.019$ | $1100 \pm 200$ | $2.0 \pm 0.2$ | $66 \pm 8$ | $0.002 \pm 0.005$ |
| Force | $6.1 \pm 0.5$ | $2.9 \pm 0.4$ | $0.110 \pm 0.017$ | $730 \pm 140$ | $4.2 \pm 0.6$ | $62 \pm 9$ | $0.002 \pm 0.011$ |

Two stopping conditions have been considered here for this process:

*(a) Displacement-driven indentation.* When the energy of a step $s$ is lower than that of the previous step [$V(h_s) < V(h_{s-1})$], the capsid has broken and the simulation stops. This scheme may correspond better to the AFM indentation experiments.

*(b) Force-driven indentation.* When the force over the roof trimers in the Z-axis direction of a step is lower than that of the previous step [$F(h_s) < F(h_{s-1})$], the capsid has broken and the simulation stops.

### B. Model fit to the experimental data and results

Some known indentation experimental AFM data about the empty MVM capsid are that it presents elastic constants of $0.58 \pm 0.13$, $0.56 \pm 0.15$ and $0.58 \pm 0.10$ N/m along the $C_5$, $C_3$ and $C_2$ symmetry axes, respectively [9], that the work of extraction of a trimer is 217 kJ/mol (this fixes the value of the $p_0$ parameter in Eq. (1) to $p_0 = 217/3$ kJ/mol), and that the average critical indentation is $h_c \sim 2$ nm [12].

To speak of elastic constants beyond the linear response regime is an abuse of language. What is meant in this context by elastic constant is the maximum of the derivative of the reaction force $F(h)$ with respect to the indentation practiced [72]. In addition, according to the VIPERdb [73,74] and taking the average radius as the interradius $r_m = 13.8$ nm, the equilibrium distance between trimers is $r_e = \frac{2}{3} r_m = 9.20$ nm. Trimers interact mainly by contact so the global minimum for 20 trimers is a regular icosahedron with a binding energy that must be very close to $V_0 = -30 p_0$.

To fit our coarse-grained interaction model to the indentation data, we define the cost function

$$\mathcal{C} = \frac{1}{5}\left[\left(1 - \frac{k_{C_2}}{k_{C_{2,t}}}\right)^2 + \left(1 - \frac{k_{C_3}}{k_{C_{3,t}}}\right)^2 + \left(1 - \frac{k_{C_5}}{k_{C_{5,t}}}\right)^2 + \left(1 - \frac{h_c}{h_{c,t}}\right)^2 + \left(1 - \frac{V_0}{V_{0,t}}\right)^2\right], \tag{6}$$

where $k_{C_2}$, $k_{C_3}$, and $k_{C_5}$ are the force constants obtained in our virtual indentation and $k_{C_{2,t}}$, $k_{C_{3,t}}$, and $k_{C_{5,t}}$ the corresponding target experimental values, $h_c$ and $h_{c,t}$ the virtual and target critical indentations, and $V_0$ and $V_{0,t} = -30 p_0$ the virtual and target binding energies, respectively.

We determine the values of the model parameter $m$, $m'$, $r_0$ and $p_1$, $p_2$, $p_3$ that provide the minimum value of the cost function. We perform this task using global optimization within the harmony search (HS) method [75]. First, we perform a random sampling of 5000 cases. Then, we feed the HS with the most optimal cases. Parameters governing HS have not been critical and 100 optimization steps along 30 trajectories have been enough to find optimal values for $\mathcal{C}$. The best fits provide values of $\mathcal{C} = 0.002$ for both displacement-driven and force-driven indentations. This implies relative errors of less than 10% between the experimental and virtual data, which are smaller that the experimental uncertainties.

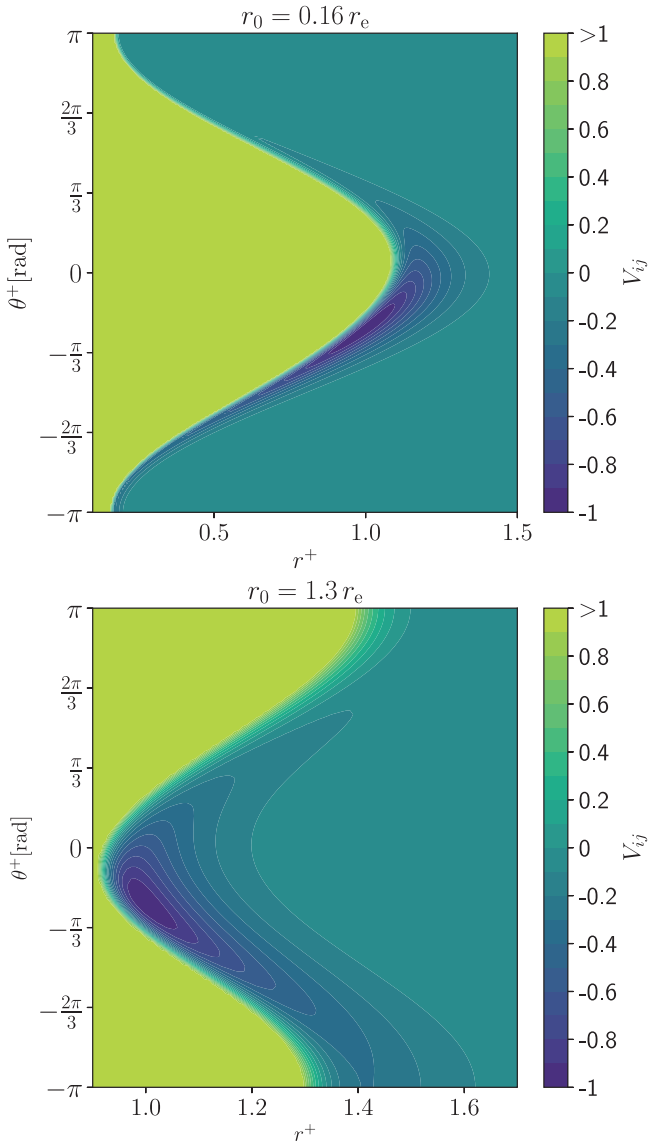


FIG. 2. Contour plots of the binary interaction $V_{ij}$ projected on the $r^+ - \theta^+$ plane, with all other internal coordinates at their equilibrium values. The top panel is obtained with the fitting parameters for MVM given in Table II and illustrates the behavior of an oblate top with $r_0 = 0.16 r_e$. The bottom panel presents the behavior of a hypothetical prolate top capsid that shares the same model parameters except for $r_0$, which is now $r_0 = 1.3 r_e$. To appreciate the valleys, only contours for $V_{ij} \leqslant 1$ are included.

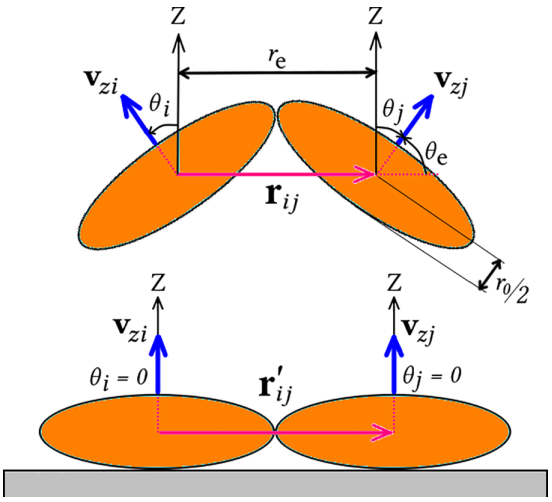


FIG. 3. Illustration of the "book-effect" after flattening a pair of oblate capsomers.

We have propagated the experimental uncertainties, assuming normal distributions for them, into the optimal model parameters by repeated minimization of the cost function for target experimental values obtained from those distributions, until a 95% of confidence level is reached. In this way, all the fitting parameters acquire the uncertainties derived from this propagation. Parameters and their uncertainties found from the fits are given in Table II.

A concerned issue is the uniqueness of the optimal parameters found so far. The propagation of the uncertainty distributions of the experimental data into the final parameter distributions that we have performed in this section may provide an answer to this issue; specifically, if several different parameter sets could compete, these would have a high probability of being sampled and would appear in the propagated parameter distributions. Instead, however, we observe that the relative parameter uncertainties found are somewhat smaller than those of the experimental data, which suggests a rather unique fit.

We observe that for both cases the easiest condition to satisfy in the optimization process is $V \simeq V_o = -30p_0$. In addition, we confirm that second-neighbor interactions are negligible and that the regular icosahedron is the global minimum configuration, as intended.

From the value of $r_0$ obtained from the fit, we conclude that trimers in MVM are quite oblate tops, in excellent agreement with their known structure. To illustrate the effect of the $r^+ - \theta^+$ coupling on the interaction energy, Fig. 2 presents contour plots of the binary interaction projected on the $r^+ - \theta^+$ plane, with all other internal coordinates at their equilibrium values.

TABLE IV. Average critical indentation $h_c$ and maximum capsid reaction forces $F_{C_i}$. Units are given within brackets, with $p_0 = 72.3$ kJ/mol and $r_e = 9.20$ nm.

| Driven by | $h_c$ [$r_e$] | $F_{C_2}$ | $F_{C_3}$ [$p_0/r_e$] | $F_{C_5}$ |
|---|---|---|---|---|
| Displacement | $0.22 \pm 0.02$ | $54 \pm 4$ | $62 \pm 8$ | $64 \pm 6$ |
| Force | $0.22 \pm 0.02$ | $57 \pm 9$ | $65 \pm 13$ | $68 \pm 8$ |

The top panel is obtained with the fitting parameters for the MVM and illustrates the behavior of a prolate top with $r_0 = 0.16r_e$. For comparison, the bottom panel presents the behavior of a hypothetical oblate top capsid that shares the same model parameters except for $r_0$, which is now $r_0 = 1.3r_e$. We may refer to the $r^+ - \theta^+$ coupling in MVM as the book effect, since the effect of this coupling is similar to the increasing separation of the book covers when a book is opened, as illustrated in Fig. 3.

Let us note that the values of the set of parameters $\{m, m', r_0, p_1, p_2, p_3\}$, and particularly $p_2$, have magnitudes significantly smaller than those found from the fit of our model to the normal mode spectrum of the STMV. Of course, these are two different viruses and comparisons between them are not completely significant. In addition, a normal mode analysis of the MVM capsid is not available. However, for the same virus, one would like to know if the indentation elastic constants derived from its normal modes correspond with those obtained from the AFM experiments, at least for small indentations. Obviously, the indentation experiments will eventually surpass the regime of linear response and the nonlinear effects will then determine the virus response. This transition from the linear to the nonlinear regimes appears to be an interesting topic of research in physical virology.

Linear and nonlinear regimes provide information on different ranges of the interaction energy, namely, the linear regime close to the equilibrium geometry in the normal-mode case and a nonlinear regime further away from equilibrium in the AFM setup. The information obtained from these two regimes is very valuable in designing more elaborate and universal forms for the functions $F_i$ in our model.

We include in Fig. 4 the curves corresponding to indentation by displacement calculated with the optimal parameters from Table II.

The elastic constants $k_{C_i}$, critical indentations $h_{C_i}$, and breakage activation energy $E_{C_i}$, axis by axis $(C_2, C_3, C_5)$, are shown in Table III. We provide in Table IV the average critical indentation $h_c$ and maximum reaction forces $F_{C_2}, F_{C_3}, F_{C_5}$. Reaction forces have not been fitted but in

TABLE III. Elastic constants $k_{C_i}$, critical indentations $h_{C_i}$, and breakage activation energy $E_{C_i}$ axis by axis $(C_2, C_3, C_5)$ from the optimal model parameters in Table II. Units are given within brackets, with $p_0 = 72.3$ kJ/mol and $r_e = 9.20$ nm.

| Driven by | $k_{C_2}$ | $k_{C_3}$ [N/m] | $k_{C_5}$ | $h_{C_2}$ | $h_{C_3}$ [$r_e$] | $h_{C_5}$ | $E_{C_2}$ | $E_{C_3}$ [$p_0$] | $E_{C_5}$ |
|---|---|---|---|---|---|---|---|---|---|
| Displacement | 0.56±0.05 | 0.55±0.10 | 0.61±0.05 | 0.190±0.010 | 0.230±0.012 | 0.219±0.010 | 5.0±0.3 | 7.0±0.5 | 7.4±0.4 |
| Force | 0.55±0.07 | 0.55±0.12 | 0.61±0.06 | 0.20±0.02 | 0.23±0.03 | 0.22±0.02 | 5.1±0.9 | 7.0±1.2 | 7.0±0.9 |

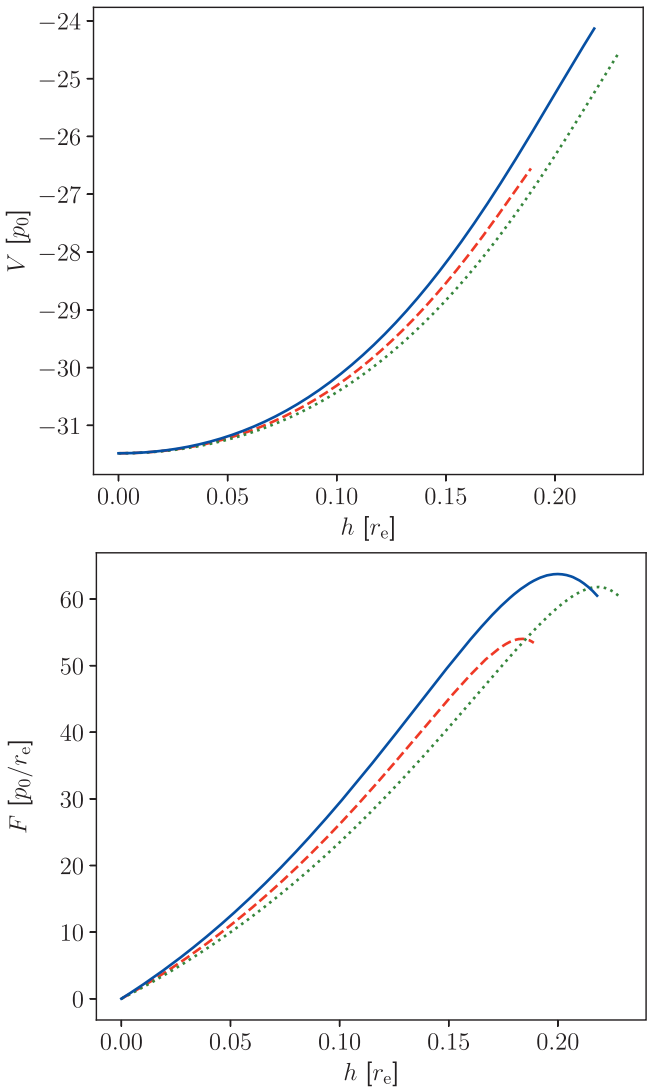


FIG. 4. Displacement-driven indentation curves of our virtual indentation of the empty MVM capsid, with the optimal model parameters in Table II. Capsid energy $V$ in $[p_0]$ units at the top and force $F$ in $[p_0/r_e]$ units at the bottom, both as functions of the indentation $h$ in $[r_e]$ units. Dashed, dotted, and continuous lines represent the indentation along the two-, three-, and fivefold symmetry axis, respectively.

Ref. [12] they range between 0.5 and 1.2 nN and, in our results, which are registered axis by axis, are about 0.75 nN.

We offer the conversion from our reduced units to SI units in Table V.

TABLE V. Conversion factors from reduced units (RUs) to SI units.

| Kind | RUs | SI | Examples |
|---|---|---|---|
| Dimensionless | 1 | 1 | $r^+, \phi^+ \ldots$ |
| Length | 1 | $r_e = 9.20 \times 10^{-9}$m | $r_0, h_{C_2} \ldots$ |
| Energy | 1 | $p_0 = 1.2006 \times 10^{-19}$J | $V, E_{C_2} \ldots$ |
| Force | 1 | $p_0/r_e = 1.3056 \times 10^{-11}$N | $F_{C_2}, F_{C_3} \ldots$ |

Once the model parameters are fixed to reproduce the experimental AFM data, we can answer important questions that are beyond the standard capabilities of typical AFM experiments. For instance, we may ask what the response of a pair of isolated trimers is when one of the internal coordinates is changed while the others remain at their equilibrium values. Specifically, we want to know what the critical value is of that coordinate that makes the binary interaction energy $V_{ij}$ vanish. That point determines the breaking point of the binary system along that coordinate. Two such critical points exist, each one corresponding to one of the two opposite directions for that coordinate. Results are shown in Table VI. These data provide valuable information about the interaction range along each of these internal coordinates.

The critical values for $r^+$ are determined by the $p_0$ term in $V_{ij}$ [Eq. (1)] and they are just the ranges of the generalized Lennar-Jones potential. The $\phi^+$ critical values are determined by the $p_1$ term in Eq. (1). The $p_3$ term in this equation determines the equal $\chi^+$ and $\chi^-$ critical values. The $p_2$ and mainly the $p_1$ term fix the $\theta^-$ critical values and the $p_2$ term affects the critical $\theta^+$ limits; the relatively small value of the parameter $p_2$ makes the coordinate $\theta^+$ have the widest range between critical values of all the angular coordinates. Besides the effect of the $r^+ - \theta^+$ coupling introduced through $\tilde{r}_e$, which is very effective because $r_0$ differs significantly from $r_e$, has extreme relevance in the indentation process by providing the main mechanism behind the capsid deformations. We have called this mechanism the book effect.

The experimental data available about this capsid has led us to choose a coarse-grained model based on trimeric subunits, which we assume to be rigid bodies. The binary trimer-trimer interaction in Eq. (1) has been able to fit rather well the AFM indentation experimental data for the MVM capsid. However, one could still ask whether other arrangements in the coarse-graining process could provide similar responses. To answer this relevant question, we have tried to fit a simpler coarse-grained model developed by our group [68] to the same AFM data. This model uses 12 rigid and axisymmetric subunits for the $T1$ capsid, each one representing a pentameric capsomer. The binary interaction is given as the minimal multipolar expansion required to produce an icosahedral $T1$ capsid from such axisymmetric subunits as the global energy minimum of the corresponding potential energy surface. This model belongs to the same class as the one proposed by Aznar *et al.* [62]. Its fit to the experimental AFM data can also be accomplished, although with somewhat larger uncertainties. One therefore concludes from these results that different arrangements of subunits and adequate interaction parameters may provide similar elastic properties. But this is not surprising: for instance, different materials and forms may provide springs with the same elastic constant. However, other details of the indentation are rather different in the trimer and pentamer models, namely, while the model with trimers provides the highest elastic constant for indentations along the fivefold axis, the model with pentamers does so along the threefold axis. Similarly, highest and lowest values of the critical indentations are obtained in both models along different axes. Of course, the pentamer model is in contradiction with the relevant role played by the trimers in the assembly and

TABLE VI. Critical deviations from equilibrium for a pair of MVM trimers along each symmetry-adapted coordinate when the rest of them are frozen at their equilibrium values. For each coordinate, the critical values for the two opposite directions are given. The binary interaction uses the fitting parameters of Table II for the optimal displacement-driven indentation.

| Direction | $r^+$ | $\phi^+$[rad] | $\theta^+$[rad] | $\chi^+$[rad] | $\theta^-$[rad] | $\chi^-$[rad] |
|---|---|---|---|---|---|---|
| Positive | $\infty$ | 0.045±0.005 | $0.35 \pm 0.03$ | 0.090±0.004 | 0.041±0.004 | 0.090±0.004 |
| Negative | $-0.105 \pm 0.005$ | −0.045±0.005 | $-2\theta_e$ | −0.090±0.004 | −0.041±0.004 | −0.090±0.004 |

disassembly of the MVM capsid [33] and should therefore be discarded. On the other hand, more accurate experimental data obtained along the three different symmetry axes could confirm the finer details obtained with the trimer model presented in this paper, and these become therefore predictions of such model. The book effect also predicted in this paper consists of an increase of the intercapsomer distance as their dihedral angle increases. A possible experimental verification of this effect could be obtained by the indentation of a pair of trimers in equilibrium along its twofold axis to observe the process illustrated in Fig. 3.

## IV. CONCLUSIONS

A minimal coarse-grained model for $T = 1$ viral capsids assembled from 20 protein trimers has been designed by extending a previously proposed form of the interaction energy written as a sum of anisotropic pairwise interactions between the rigid trimeric subunits.

The two-capsomer interaction has a twofold symmetry axis and, as a consequence, the six internal coordinates can be defined as either symmetric or antisymmetric with respect to a rotation of $\pi$ around that axis.

The extension of the model has been performed to properly account for the coupling between the symmetric internal coordinates $r^+$ (intercapsomer distance) and $\theta^+$ (intercapsomer dihedral angle).

The model has been able to fit with less than a 10% error the AFM indentation experimental data for the empty capsid of the MVM. The statistical propagation of the experimental uncertainties points to a rather unique fit. In this way, these results provide an admissible picture of the main mechanism behind the capsid deformations. In this picture, the bending coordinate $\theta^+$ is the angular internal coordinate that can support larger deformations away from its equilibrium values, determining important features of the AFM indentation experiments as the elastic constants and the critical indentation. With increasing rigidity, one finds the other angular coordinates $\chi^+$ and $\chi^-$, $\phi^+$, and, finally, the most rigid antisymmetric $\theta^-$ coordinate.

The coarse-grained model is able to provide important predictions, namely, the critical indentation is larger along the $C_3$ symmetry axis and smaller along the $C_2$ axis. On the other hand, the elastic constant is higher along the $C_5$ axis and lower along the $C_2$ and $C_3$ axes. Therefore, the bending $\theta^+$ mode appears to participate in a more dominant way in the indentation along the $C_3$ symmetry axes of the capsid. These predictions of our model would require more accurate experimental data to be confirmed.

From the value of $r_0$ obtained from the fit, we conclude that trimers in MVM are quite oblate tops, in excellent agreement with their known structure in VIPERdb. For this top, the internal coordinate $r^+$ increases or decreases as $\theta^+$ does. This is the book effect that originates in the $r^+ - \theta^+$ coupling; without this effect, the critical indentations would be significantly smaller.

The AFM experiments sample a region of capsid potential energy surface beyond the linear regime that characterizes the vibrational normal modes of the capsid, with effective elastic constants that may be significantly smaller than those corresponding to the linear regime. The transition from the linear to the nonlinear regimes appears to be an interesting topic for future research in physical virology. It has been shown that the minimal coarse-grained model presented in this paper can be adjusted with the book effect to fit these two regimes in $T = 1$ capsids and, in this way, to provide valuable information on the physical mechanisms behind the capsid dynamical and elastic responses.

## ACKNOWLEDGMENTS

This work was funded by the Spanish Ministerio de Ciencia e Innovación through Grant No. PID2019-105225GB-I00/AEI/10.13039/501100011033 (MICINN/FEDER, UE). M.M.-B. thanks the Spanish Ministerio de Economía y Competitividad (MINECO) for the predoctoral Grant No. BES-2017-081104.

[1] S. Bhaskar and S. Lim, NPG Asia Mater. **9**, e371 (2017).
[2] S. Xie, L. Ai, C. Cui, T. Fu, X. Cheng, F. Qu, and W. Tan, ACS Appl. Mater. Interfaces **13**, 9542 (2021).
[3] X. Yu, Z. Weng, Z. Zhao, J. Xu, Z. Qi, and J. Liu, Pharmaceutics **14**, 2609 (2022).
[4] I. L. Ivanovska, P. J. de Pablo, B. Ibarra, G. Sgalari, F. C. MacKintosh, J. L. Carrascosa, C. F. Schmidt, and G. J. L. Wuite, Proc. Natl. Acad. Sci. USA **101**, 7600 (2004).
[5] W. H. Roos, M. M. Gibbons, A. Arkhipov, C. Uetrecht, N. R. Watts, P. T. Wingfield, A. C. Steven, A. J. R. Heck, K. Schulten, W. S. Klug, and G. J. L. Wuite, Biophys. J. **99**, 1175 (2010).
[6] Y. Guo and W. H. Roos, AFM nanoindentation experiments on protein shells: A protocol, in *Atomic Force Microscopy*, edited by N. Santos and F. Carvalho, Methods in Molecular Biology (Humana Press, New York, NY, 2019), Vol. 1886.
[7] M. R. Falvo, S. Washburn, R. Superfine, M. Finch, F. P. Brooks, Jr., V. Chi, and R. M. Taylor, II, Biophys. J. **72**, 1396 (1997).

[8] J. P. Michel, I. L. Ivanovska, M. M. Gibbons, W. S. Klug, C. M. Knobler, G. J. L. Wuite, and C. F. Schmidt, Proc. Natl. Acad. Sci. USA **103**, 6184 (2006).

[9] C. Carrasco, A. Carreira, I. A. T. Schaap, P. A. Serena, J. Gómez-Herrero, M. G. Mateu, and P. J. de Pablo, Proc. Natl. Acad. Sci. USA **103**, 13706 (2006).

[10] C. Carrasco, M. Castellanos, P. J. de Pablo, and M. G. Mateu, Proc. Natl. Acad. Sci. USA **105**, 4150 (2008).

[11] I. L. Ivanovska, R. Miranda, J. L. Carrascosa, G. J. L. Wuite, and C. F. Schmidt, Proc. Natl. Acad. Sci. USA **108**, 12611 (2011).

[12] M. Castellanos, R. Pérez, P. J. P. Carrillo, P. J. de Pablo, and M. G. Mateu, Biophys. J. **102**, 2615 (2012).

[13] M. Castellanos, R. Pérez, C. Carrasco, M. Hernando-Pérez, J. Gómez-Herrero, P. J. de Pablo, and M. G. Mateu, Proc. Natl. Acad. Sci. USA **109**, 12028 (2012).

[14] R. Zandi and D. Reguera, Phys. Rev. E **72**, 021917 (2005).

[15] W. S. Klug, R. F. Bruinsma, J.-P. Michel, C. M. Knobler, I. L. Ivanovska, C. F. Schmidt, and G. J. L. Wuite, Phys. Rev. Lett. **97**, 228101 (2006).

[16] M. M. Gibbons and W. S. Klug, Biophys. J. **95**, 3640 (2008).

[17] M. Zink and H. Grubmüller, Biophys. J. **96**, 1350 (2009).

[18] A. Ahadi, J. Colomo, and A. Evilevitch, J. Phys. Chem. B **113**, 3370 (2009).

[19] A. Arkhipov, W. H. Roos, G. J. L. Wuite, and K. Schulten, Biophys. J. **97**, 2061 (2009).

[20] M. Cieplak and M. O. Robbins, J. Chem. Phys. **132**, 015101 (2010).

[21] A. Zhmurov, K. Rybnikov, Y. Kholodov, and V. Barsegov, J. Phys. Chem. B **115**, 5278 (2011).

[22] E. R. May and C. L. Brooks, J. Phys. Chem. B **116**, 8604 (2012).

[23] M. Cieplak and M. O. Robbins, PLoS ONE **8**, e63640 (2013).

[24] K. J. Boyd, P. Bansal, J. Feng, and E. R. May, Front. Bioeng. Biotechnol. **3**, 1 (2015).

[25] C. Carrasco, A. Luque, M. Hernando-Pérez, R. Miranda, J. L. Carrascosa, P. A. Serena, M. de Ridder, A. Raman, J. Gómez-Herrero, I. A. T. Schaap, D. Reguera, and P. J. de Pablo, Biophys. J. **100**, 1100 (2011).

[26] O. Kononova, J. Snijder, M. Brasch, J. Cornelissen, R. I. Dima, K. A. Marx, G. J. L. Wuite, W. H. Roos, and V. Barsegov, Biophys. J. **105**, 1893 (2013).

[27] F. Maksudov, O. Kononova, A. Llauró, A. Ortega-Esteban, T. Douglas, G. N. Condezo, C. S. Martín, K. A. Marx, G. J. L. Wuite, W. H. Roos, P. J. de Pablo, and V. Barsegov, Acta Biomater. **122**, 263 (2021).

[28] W. H. Roos, I. L. Ivanovska, A. Evilevitch, and G. J. L. Wuite, Cell. Mol. Life Sci. **64**, 1484 (2007).

[29] M. G. Mateu, Virus Res. **168**, 1 (2012).

[30] P. J. de Pablo and M. G. Mateu, Mechanical properties of viruses, in *Structure and Physics of Viruses: An Integrated Textbook*, edited by M. G. Mateu (Springer Netherlands, Dordrecht, 2013), pp. 519–551.

[31] R. Zandi, B. Dragnea, A. Travesset, and R. Podgornik, Phys. Rep. **847**, 1 (2020).

[32] P. Buzón, S. Maity, and W. H. Roos, Wiley Interdiscip. Rev.: Nanomed. Nanobiotechnol. **12**, e1613 (2020).

[33] M. Medrano, M. A. Fuertes, A. Valbuena, P. J. P. Carrillo, A. Rodríguez-Huete, and M. G. Mateu, J. Am. Chem. Soc. **138**, 15385 (2016).

[34] E. Lombardo, J. C. Ramírez, M. Agbandje-McKenna, and J. M. Almendral, J. Virol. **74**, 3804 (2000).

[35] E. Lombardo, J. C. Ramírez, J. Garcia, and J. M. Almendral, J. Virol. **76**, 7049 (2002).

[36] L. Riolobos, J. Reguera, M. G. Mateu, and J. M. Almendral, J. Mol. Biol. **357**, 1026 (2006).

[37] R. Pérez, M. Castellanos, A. Rodríguez-Huete, and M. G. Mateu, J. Mol. Biol. **413**, 32 (2011).

[38] H. D. Nguyen, V. S. Reddy, and C. L. Brooks, Nano Lett. **7**, 338 (2007).

[39] R. Zandi, D. Reguera, R. F. Bruinsma, W. M. Gelbart, and J. Rudnick, Proc. Natl. Acad. Sci. USA **101**, 15556 (2004).

[40] A. Luque, R. Zandi, and D. Reguera, Proc. Natl. Acad. Sci. USA **107**, 5323 (2010).

[41] R. F. Bruinsma, W. M. Gelbart, D. Reguera, J. Rudnick, and R. Zandi, Phys. Rev. Lett. **90**, 248101 (2003).

[42] A. Luque, D. Reguera, A. Morozov, J. Rudnick, and R. Bruinsma, J. Chem. Phys. **136**, 184507 (2012).

[43] T. Chen, Z. Zhang, and S. C. Glotzer, Proc. Natl. Acad. Sci. USA **104**, 717 (2007).

[44] T. Chen and S. C. Glotzer, Phys. Rev. E **75**, 051504 (2007).

[45] S. Li, P. Roy, A. Travesset, and R. Zandi, Proc. Natl. Acad. Sci. USA **115**, 10971 (2018).

[46] B. Berger, P. W. Shor, L. Tucker-Kellogg, and J. King, Proc. Natl. Acad. Sci. USA **91**, 7732 (1994).

[47] R. Schwartz, P. W. Shor, P. E. Prevelige Jr., and B. Berger, Biophys. J. **75**, 2626 (1998).

[48] D. J. Wales, Phys. Biol. **2**, S86 (2005).

[49] D. C. Rapaport, Phys. Rev. E **70**, 051905 (2004).

[50] H. D. Nguyen and C. L. Brooks, Nano Lett. **8**, 4574 (2008).

[51] S. N. Fejer, T. R. James, J. Hernández-Rojas, and D. J. Wales, Phys. Chem. Chem. Phys. **11**, 2098 (2009).

[52] M. F. Hagan and D. Chandler, Biophys. J. **91**, 42 (2006).

[53] K. V. Workum and J. F. Douglas, Phys. Rev. E **73**, 031502 (2006).

[54] O. M. Elrad and M. F. Hagan, Nano Lett. **8**, 3850 (2008).

[55] S. N. Fejer, D. Chakrabarti, and D. J. Wales, ACS Nano **4**, 219 (2010).

[56] K. Peeters and A. Taormina, Comput. Math. Methods Med. **9**, 211 (2008).

[57] B. H. Lee, S. Jo, M. ki Choi, M. H. Kim, J. B. Choi, and M. K. Kim, Comput. Biol. Chem. **72**, 53 (2018).

[58] M. Widom, J. Lidmar, and D. R. Nelson, Phys. Rev. E **76**, 031911 (2007).

[59] Z. Yang, I. Bahar, and M. Widom, Biophys. J. **96**, 4438 (2009).

[60] A. Levandovsky and R. Zandi, Phys. Rev. Lett. **102**, 198102 (2009).

[61] A. L. Božič, A. Šiber, and R. Podgornik, J. Biol. Phys. **39**, 215 (2013).

[62] M. Aznar, S. Roca-Bonet, and D. Reguera, J. Phys.: Condens. Matter **30**, 264001 (2018).

[63] C. Tiwari, V. Sharma, P. K. Jha, and A. Pratap, J. Biomol. Struct. Dyn. **38**, 2207 (2019).

[64] M. Martín-Bravo, J. M. Gomez Llorente, and J. Hernández-Rojas, Soft Matter **16**, 3443 (2020).

[65] M. Martín-Bravo, J. M. Gomez Llorente, J. Hernández-Rojas, and D. J. Wales, ACS Nano **15**, 14873 (2021).

[66] M. K. Kim, R. L. Jernigan, and G. S. Chirikjian, J. Struct. Biol. **143**, 107 (2003).

[67] Y.-C. Hsieh, F. Poitevin, M. Delarue, and P. Koehl, Front. Mol. Biosci. **3**, 85 (2016).
[68] J. M. Gomez Llorente, J. Hernández-Rojas, and J. Bretón, Soft Matter **10**, 3560 (2014).
[69] M. Aznar and D. Reguera, J. Phys. Chem. B **120**, 6147 (2016).
[70] D. Reguera, J. Hernández-Rojas, and J. M. Gomez Llorente, Soft Matter **15**, 7166 (2019).
[71] D. Wales, *Energy Landscapes: Applications to Clusters, Biomolecules and Glasses*, Cambridge Molecular Science (Cambridge University Press, United Kingdom, 2004).
[72] G. A. Vliegenthart and G. Gompper, Biophys. J. **91**, 834 (2006).
[73] https://viperdb.org.
[74] D. Montiel-Garcia, N. Santoyo-Rivera, P. Ho, M. Carrillo-Tripp, C. L. Brooks III, J. E. Johnson, and V. S. Reddy, Nucleic Acids Res. **49**, D809 (2021).
[75] Z. W. Geem, J. H. Kim, and G. V. Loganathan, Simulation **76**, 60 (2001).